RSC Advances

PAPER

View Article Online
View Journal | View Issue

Cite this: *RSC Adv.*, 2022, **12**, 20348

Optical and dielectric properties of silver-substituted $ZnAl_2O_4$ spinels synthesized using a sol-gel auto-combustion method

Mohamed Amghar, *[a] Amira Bougoffa, [a] Abdessalem Trabelsi,[a] Abderrazek Oueslati [b] and Essebti Dhahri [a]

The present study deals with two compounds, $Ag_xZn_{1-x}Al_2O_{4-\frac{x}{2}}$ ($x = 0.05$ and $x = 0.1$), synthesized using a sol-gel auto-combustion method. X-ray diffraction analysis and Fourier transform infrared spectroscopy confirmed the formation of a spinel structure. UV-visible spectroscopy revealed that the band gap is 4.3 eV and 4 eV for $x = 0.05$ and $x = 0.1$, respectively, which confirm that these compounds, $Ag_xZn_{1-x}Al_2O_{4-\frac{x}{2}}$ ($x = 0.05$ and $x = 0.1$), are potential candidates for optoelectronics. Moreover, the effect of frequency and temperature on the dielectric parameters was studied using impedance spectroscopy. Additionally, the activation energies were estimated from the modulus data and are about 0.659 eV for $x = 0.05$ and 0.41 eV for $x = 0.1$. These values are in good agreement with those obtained from complex polarizability.

Received 21st April 2022
Accepted 3rd July 2022

DOI: 10.1039/d2ra02555h

rsc.li/rsc-advances

1. Introduction

In ceramics, the family of spinels with the general chemical formula AB_2O_4, where A denotes a divalent metal ion with tetrahedral symmetry and B denotes a trivalent metal ion with octahedral symmetry, are an ideal type of material for forming ternary oxides thanks to their electrical, optical, magnetic, and mechanical properties.[1] Aluminum-based spinels, MAl_2O_4 M(Mg, Zn, Co), have attracted attention, given their exceptional physical properties, including a high melting point, high mechanical resistance at high temperature, resistance to radiation damage, low permittivity, and low loss tangent. As a result, they have demonstrated potential for use in a large range of applications.[2] Furthermore, polycrystalline zinc aluminate ($ZnAl_2O_4$) has an optical band gap of 3.8 to 3.9 eV.[3–5] Thus, it can be used for ultraviolet (UV) photoelectronic devices thanks to its transparency and electrical conductive properties.[6] In fact, $ZnAl_2O_4$ with a normal spinel structure is one of such compounds, and it is used in a variety of catalytic reactions namely dehydration, hydrogenation, and cracking in the chemical and petrochemical industries.[7] Relying on its excellent optical and hydrophobic properties, and high chemical and thermal stability, it is also used in optoelectronics, sensor technology, and information display technology as an effective phosphor material for flat panel displays.[8] The latter are widely used in millimeter-wave telecommunication systems, especially in antennas, dielectric resonators and microwave substrate applications as a consequence of their low dielectric constant, and high-quality factor.[9] Let us recall that, solid-state reaction,[10] sol-gel,[11] co-precipitation,[12] microwave hydrothermal,[13] solvothermal,[14] hydrothermal[15] and combustion methods were commonly used to produce these compounds.[16] Interstingy, doping zinc aluminum with rare earth[17] gives photophysical properties that could be used in upconversion lasers. $ZnAl_2O_4$-doped nickel and cobalt are widely used as blue and green-blue pigments in glass and ceramics.[18] Therefore, the main objective of this contribution is to study the optical and dielectric properties of the Ag^+ doped $ZnAl_2O_4$ compounds.

With this in mind, X-ray diffractometer (XRD) measurements, Fourier transform infrared spectroscopy (FTIR), UV-vis scattered reflectance spectroscopy, and impedance spectroscopy carried out at several temperatures ranging from 313 to 653 K in the frequency range of 0.1 Hz to 1 MHz, were used to characterize the prepared nanomaterials.

2. Experimental

0.07 g Silver nitrate (99.8% purity, Sigma-Aldrich), 0.63 g Zinc oxide (98% purity, Sigma-Aldrich), and 6.07 g Aluminum nitrate (98% purity, Sigma-Aldrich) were used as precursors to prepare the $Ag_xZn_{1-x}Al_2O_{4-\frac{x}{2}}$ samples by the sol-gel auto-combustion method.[19] All precursors were dissolved in distilled water (50 ml). After that, 5.76 g citric acid (98% purity) was added. An homogeneous solution was obtained, then heated at 80 °C to

[a]*Laboratory of Applied Physics, Faculty of Sciences of Sfax, University of Sfax, B. P. 1171, Sfax, 3000, Tunisia. E-mail: amgharmohamed498@gmail.com*
[b]*Laboratory of Spectroscopic Characterization and Optic Materials, University of Sfax, Faculty of Sciences of Sfax, B.P. 1171, Sfax, 3000, Tunisia*

reach a viscose: gel solution. Later, the obtained gel was heated on a hot plate at 180 °C until powders are formed. Subsequently resulting powders were calcined in the air at 350 °C, 500 °C, and 700 °C for six hours to evaporate the solvent. In the final step, the powders were pressed into pellets of 8 mm in diameter, and sintered at 800 °C for twenty four hours to induce the crystallization of the samples. These samples were characterized by X-ray diffraction at room temperature with an Advanced D8 diffractometer and monochromatic CuKα radiation (λ = 1.5406 Å). Fourier Transform Infrared (FTIR) spectra were recorded using a PerkinElmer FTIR-1000 spectrophotometer in the wavenumber range of 400 to 4000 cm^{-1}. The diffuse reflectance UV-visible spectra of compounds were registered using a SHIMADZU spectrophotometer (UV-3101 PC) in the 200–1100 nm wavelength range. The dielectric characteristics of the samples were obtained by impedance spectroscopy at different temperatures of 313 to 653 K over a frequency range of 0.1 Hz to 1 MHz using an Agilent 4294 impedance analyzer.

3. Results and discussion

3.1 X-ray diffraction analysis

The X-ray diffraction patterns of $Ag_xZn_{1-x}Al_2O_{4-\frac{x}{2}}$ (x = 0.05 and x = 0.1) samples, prepared by sol-gel auto-combustion method, are displayed in Fig. 1. The observed diffraction peaks in the two recorded XRD patterns correspond to those of the standard patterns of cubic $ZnAl_2O_4$ spinel. In addition, we notice a minority phase attributed to silver metal (Ag), as detailed in our previous work.[19]

3.2 Fourier Transform Infrared (FTIR) analysis

The FTIR spectroscopy, which is a useful tool to understand functional groups in materials, which have been recorded in the range of 4000–400 cm^{-1}. Fig. 2 depicts the FT-IR spectra of $Ag_xZn_{1-x}Al_2O_{4-\frac{x}{2}}$ (x = 0.05 (a) and x = 0.1 (b)), respectively. The broad band at 3433 cm^{-1} can be attributed to the O–H longitudinal stretching vibration of water molecules, whilst the band from 1625 cm^{-1} is attributed to the band vibration of H–O–H.[20,21] The three main bands around 676, 567 and 511 cm^{-1} attributed to the tetrahedral and octahedral of the spinel[22–25] confirming thus the formation of the spinel as previously shown by XRD results.[26]

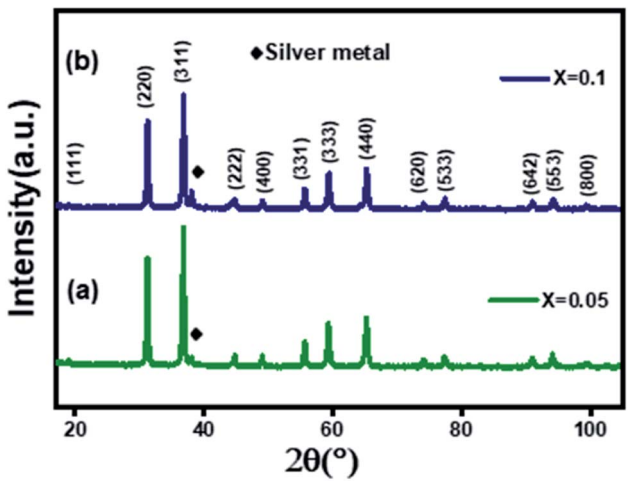

Fig. 1 XRD patterns of $Ag_xZn_{1-x}Al_2O_{4-\frac{x}{2}}$ (x = 0.05 (a) and x = 0.1 (b)) nanoparticles.

3.3 UV-vis spectra and optical band gap studies

The fundamental process of absorption, reflection, or transmission of light in the materials is considered relevant for their electronic structures. The reflectance spectra of the prepared samples are plotted in Fig. 3a and b. The spectra were recorded in the spectral range between 250 and 1000 nm. Two absorption bands in the UV region, centered around 281 and 379 nm, are visible in the samples, which could be assigned to band-to-band absorption and host material defects.[27]

The energy bandgap mainly comes from the charge jump from the valence band to the conduction band estimaed using Tauc's relationship:[28]

$$(F(R)h\nu) = A(h\nu - E_g)^n \quad (1)$$

where E_g is the optical band gap energy of materials, A is a constant, $h\nu$ is the photon energy, and n is a coefficient equal to either 1/2 for indirect band gap or 2 for direct band gap.

The diffuse reflectance data were used to calculate the absorption coefficient from the Kubelka–Munk (KM)[29] function, which was defined as follows:

$$F(R) = \frac{(1-R)^2}{2R} \quad (2)$$

where R denotes reflectance, and $F(R)$ represents the Kubelka–Munk function.

Knowing that the pure and doped $ZnAl_2O_4$ compound has a direct transition, the value of the exponent n is 2, as in the literature.[30–33]

Fig. 4 displays the plot of $(F(R)h\nu)^2$ *versus* photon energy ($h\nu$) for the samples $Ag_xZn_{1-x}Al_2O_{4-\frac{x}{2}}$ (x = 0.05 (a) and x = 0.1 (b)). Extrapolation of the linear part of the plot of $(F(R)h\nu)^2$ as a function of photon energy ($h\nu$) gives an estimate of the energy band gap. The recently reported direct band gap values for the compounds $Ag_xZn_{1-x}Al_2O_{4-\frac{x}{2}}$ were 4.3 eV and 4 eV for x = 0.05 and x = 0.1, respectively. Indicating the semiconductor character, this material is suitable for specific applications such as photodetectors, optoelectronics, and photovoltaics.[34–36]

With Ag substitution, E_g values decrease when x increases. This reduction can be attributed to the increased levels of deep defects caused by Ag doping. Consequently, Ag-substituted $ZnAl_2O_4$ absorbs more photons and generates more electrons and holes, favoring photocatalytic activity.[37]

The metallization criterion (M) is usually used to predict the conductivity behavior of solids, where: $M = \sqrt{\frac{E_g}{20}}$[28]

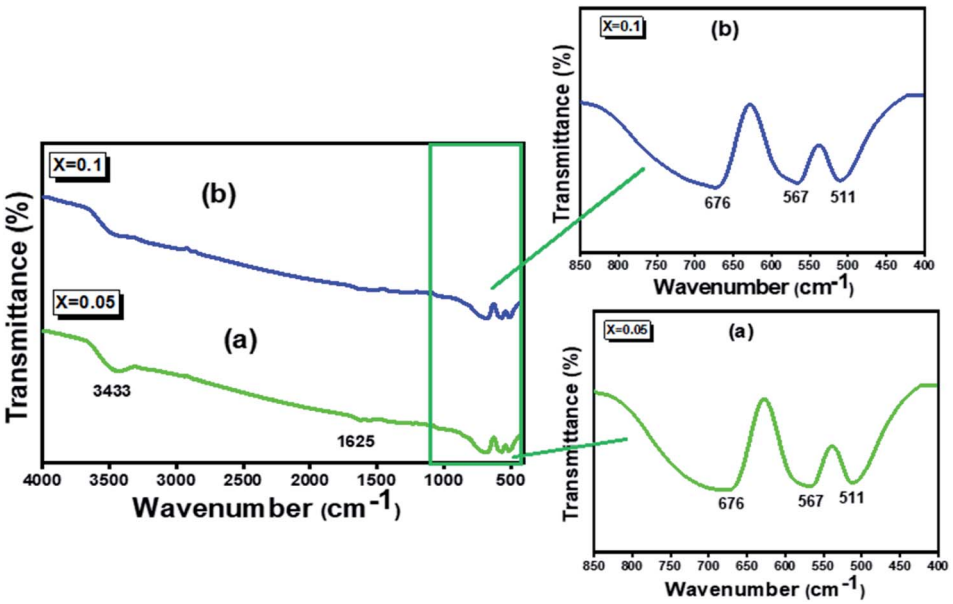

Fig. 2 FT-IR spectra of the $Ag_xZn_{1-x}Al_2O_{4-\frac{x}{2}}$ ($x = 0.05$ (a) and $x = 0.1$ (b)) samples.

When M reaches a high value, close to 1, it means that the material behaves like an insulator. While it shows a more metallic character when M approaches 0.[38]

In the current work, the values of the metallization criterion were found to vary from 0.46 to 0.44 $(eV)^{0.5}$ for $x = 0.05$ and $x = 0.1$, respectively, reflecting the semiconducting character of these samples.[39]

Besides, the refractive index (n_0) of semiconducting materials is very important to evaluate their optical and electrical properties especially for optoelectronic and solar cell devices.[40]

The refractive index (n_0) can be calculated from the value of E_g using Moss empirical relation:[41]

$$E_g n_0^4 = 104 \text{ eV} \quad (3)$$

Furthermore, we have calculated the high-frequency dielectric constant ε_α with a refractive index by using the following relation:[42]

$$\varepsilon_\alpha = n_0^2$$

The calculated values relative to n_0 and ε_α are for $= 0.05$: $n_0 = 2.22$ and $\varepsilon_\alpha = 4.93$ and for $x = 0.1$: $n_0 = 2.26$ and $\varepsilon_\alpha = 5.11$.

3.4 Dielectric study

The permittivity measurements were performed to investigate the dielectric properties of the prepared samples. The complex dielectric permittivity can be expressed according to Mott's theory by the following equation:[43]

$$\varepsilon^* = \varepsilon' - i\varepsilon'' = \frac{1}{i\omega C_0 Z^*} \quad (5)$$

where: $\omega = 2\pi f$ is the angular frequency, C_0 is the open capacity of the capacitor, and ε' (ε''), is the real (imaginary) part of the dielectric permittivity.

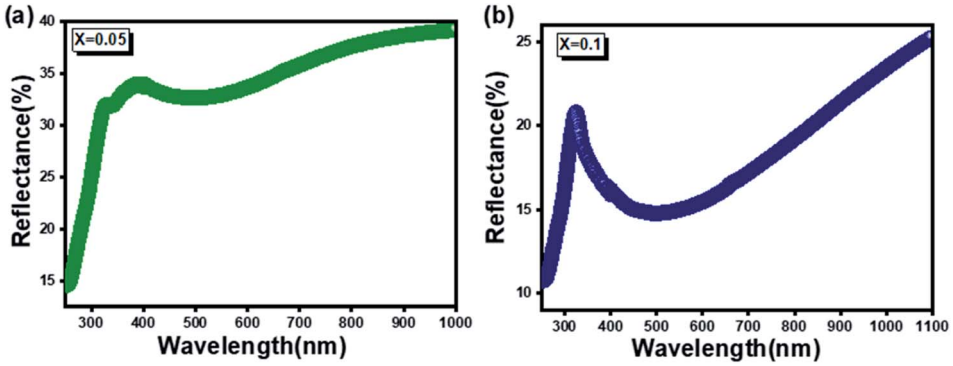

Fig. 3 Diffuse reflectance spectra of $Ag_xZn_{1-x}Al_2O_{4-\frac{x}{2}}$ ($x = 0.05$ (a) and $x = 0.1$ (b)) compounds.

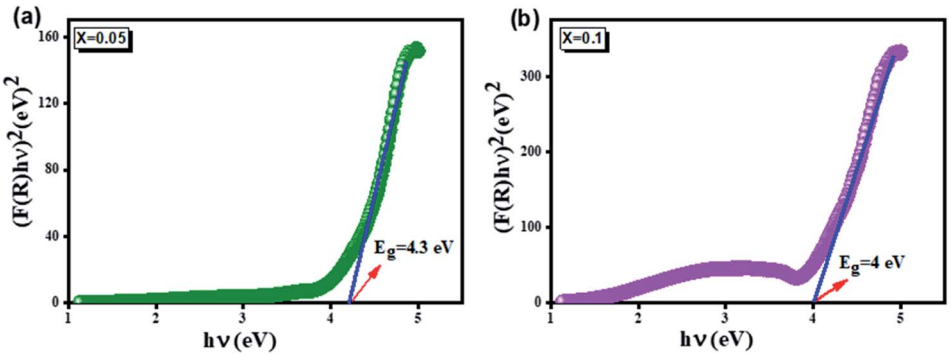

Fig. 4 Plot of $(F(R)h\nu)^2$ *versus* $(h\nu)$ for $Ag_xZn_{1-x}Al_2O_{4-\frac{x}{2}}$ ($x = 0.05$ (a) and $x = 0.1$ (b)) samples.

3.4.1 Real part of dielectric permittivity. Fig. 5a and b presents the spectra of the real permittivity (ε') over a wide range of frequencies at different temperatures for the samples $Ag_xZn_{1-x}Al_2O_{4-\frac{x}{2}}$ ($x = 0.05$ and $x = 0.1$). It can be noted that ε' increases with decreasing frequency and increasing temperature for both samples, this finding specifies strong dielectric dispersion. This independence is due to the disability of the electric dipoles to follow the rapid variation of the applied electric field. Indeed, the high value of ε' at low frequencies is mainly linked to the supply of electronic, spatial, interfacial and ionic charges, which are generally accompanied by the appearance of dielectric relaxation. Therefore, the dielectric dispersion observed in the low-frequency region is attributed to interfacial polarization, since electronic and atomic polarizations remain unchanged in this frequency range.[44] Since dipoles are not able to orient themselves at low temperature, the increase in ε' with temperature is associated to the fact that orientation polarization is related to the thermal motion of molecules.[45]

The experimental data of the dielectric constant (ε') were adjusted using the modified Debye function given by the following expression:[46]

$$\varepsilon' = \varepsilon'_{\infty} + \frac{\varepsilon'_0 - \varepsilon'_{\infty}}{\left[1 + (\omega\tau)^{2(1-\alpha)}\right]} \quad (6)$$

with: τ is the average relaxation time, α is a constant, ε'_0 is the dielectric constant at low frequency, and ε'_{∞} is the dielectric constant at high frequency.

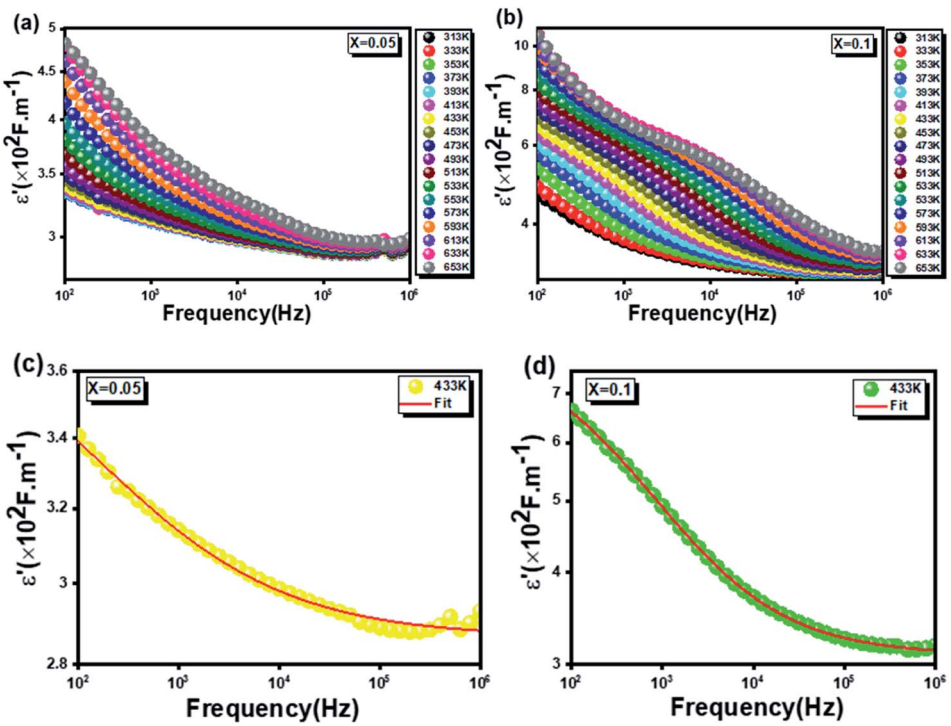

Fig. 5 The real permittivity spectra over a wide range of frequencies at different temperatures for the $Ag_xZn_{1-x}Al_2O_{4-\frac{x}{2}}$ ($x = 0.05$ (a) and $x = 0.1$ (b)) nanoparticles. Example fit of the (ε') for ($x = 0.05$ (c) and $x = 0.1$ (d)) at $T = 433$ K.

Table 1 The extracted fitting parameters of the dielectric constant for samples (a) $x = 0.05$ and (b) $x = 0.1$

T(K)	ε'_∞	ε'_0	$\tau(\times 10^{-4}$ s)	α
a				
313	286.228	533.030	197.9	0.606
333	285.477	449.166	110.5	0.597
353	286.219	381.550	14.8	0.612
373	286.580	370.775	9.491	0.619
393	286.783	367.731	7.788	0.623
413	287.049	364.857	6.308	0.627
433	287.857	358.106	3.642	0.643
453	287.500	384.279	9.158	0.624
473	289.088	354.958	1.981	0.671
493	289.146	379.135	4.182	0.651
513	289.837	396.356	4.990	0.652
533	291.152	391.738	2.721	0.680
553	291.540	392.361	1.607	0.698
573	292.296	408.412	1.529	0.708
593	294.162	448.053	2.451	0.697
613	295.173	486.198	3.086	0.688
633	296.124	507.949	2.919	0.685
653	295.475	499.068	1.932	0.680
b				
313	303.380	2229.150	3242.1	0.611
333	305.182	1813.746	1158.4	0.617
353	305.462	1584.427	365.2	0.622
373	307.185	960.237	31.1	0.636
393	308.175	854.618	11.4	0.645
413	309.128	819.915	6.217	0.651
433	309.299	814.972	4.141	0.652
453	309.151	825.538	3.019	0.651
473	307.325	852.730	2.458	0.644
493	304.109	889.698	2.146	0.636
513	297.307	958.701	2.226	0.623
533	284.217	1071.842	2.984	0.606
553	287.775	1072.210	2.085	0.609
573	280.154	1135.673	2.174	0.602
593	275.466	1344.296	4.815	0.591
613	281.412	1170.767	1.666	0.599
633	298.463	1311.502	3.425	0.596
653	314.602	1193.628	2.113	0.607

As clearly seen from Fig. 5c and d, the theoretical fit is strongly agree with the experimental data indicating the adequacy of the used modified Debye function. In this regard, the extracted parameters from the fitting process for the two studied compounds are illustrated in Table 1.

3.4.2 Imaginary part of dielectric permittivity. Fig. 6 exhibits the variation of the imaginary part (ε'') of the complex permittivity *versus* frequency at different temperatures for the two compounds $Ag_xZn_{1-x}Al_2O_{4-\frac{x}{2}}$ ($x = 0.05$ (a) and $x = 0.1$ (b)), respectively. It is clear that ε'' presents high values in the low-frequency region and decreases rapidly with increasing frequency within the presence of any relaxation peak. This feature is indicative of non-Debey behavior.[47]

In addition, as seen in Fig. 6c and d, the imaginary part of dielectric constant (ε'') can be represented in a logarithmic variation $\ln(\varepsilon'')$ as a function of $\ln(\omega)$ at different temperatures according to the following expression given by Giuntini *et al.*:[48]

$$\varepsilon''(\omega) = (\varepsilon_s - \varepsilon_\infty)2\pi^2 \cdot N\left(\frac{n \cdot e^2}{\varepsilon_0}\right)^3 K_B T \cdot \omega^m \cdot \tau_0{}^m \cdot (W_M)^{-4} \quad (7)$$

Which can be rephrased as follows:[49]

$$\varepsilon'' = B(T) \cdot \omega^{m(T)} \quad (8)$$

In eqn (7), ε_s is the static dielectric constant, ε_∞ the dielectric constant at "infinitely high" frequencies, K_B is Boltzmann's constant, N is the density of localized states at which carriers exist, n is the number of polarons involved in the charge transfer process, e is an electronic charge, and W_M is the energy required to move the electron from site to infinity (that's to say the energy necessary for charge carriers to cross over the potential barrier).

Then, in eqn (8), $B(T)$ is a constant that depends only on temperature and m denotes an exponent describing the number of charge carriers, which is given by:[50]

$$m = -\frac{4K_B T}{W_M} \quad (9)$$

The calculated values of m as a function of temperature are collated in Fig. 7a and b. The same type of evolution has been observed in other compounds.[51,52]

As shown in Fig. 7a and b, for $x = 0.05$, the values of m are proportional to the temperature, which matches the non-overlapping small polaron tunneling (NSPT)[53] model, and then decrease with increasing temperature, suggesting the (CBH) model. Nevertheless, for $x = 0.1$, it is clear that m decreases with increasing temperature. Therefore, the correlated barrier hopping (CBH) model is the predominant mechanism. These findings are in good agreement with our previously published results regarding the electrical investigation of these two material.[19]

The temperature dependence of the real ε' and imaginary ε'' permittivity as a function of temperature at different frequencies (0.1 KHz, 1 KHz, 10 KHz, and 1 MHz) for the two compounds is illustrated in Fig. 8 and 9. As clearly seen, ε' and ε'' are independent of frequencies and temperatures over a small temperature range, then they gradually increase as the temperature increases. Furthermore, the interfacial polarization is known, as it increases with increasing temperature while the dipole polarization decreases with temperature.[54,55] The observed increase in dielectric constant with the temperature at low frequencies confirms the domination of the interfacial polarization contribution to the dielectric constant in the studied materials.[56]

3.4.3 Loss factor. The dielectric loss factor expresses the ratio of the imaginary part of dielectric permittivity (ε'') and the real part of dielectric permittivity (ε'), *i.e.*:

$$\tan\delta = \frac{\varepsilon''}{\varepsilon'} \quad (10)$$

where the angle δ is the phase difference between the applied electric field and the induced current.

Dielectric loss is known to occur when bias lags behind the applied AC field and can be caused by defects in the crystal

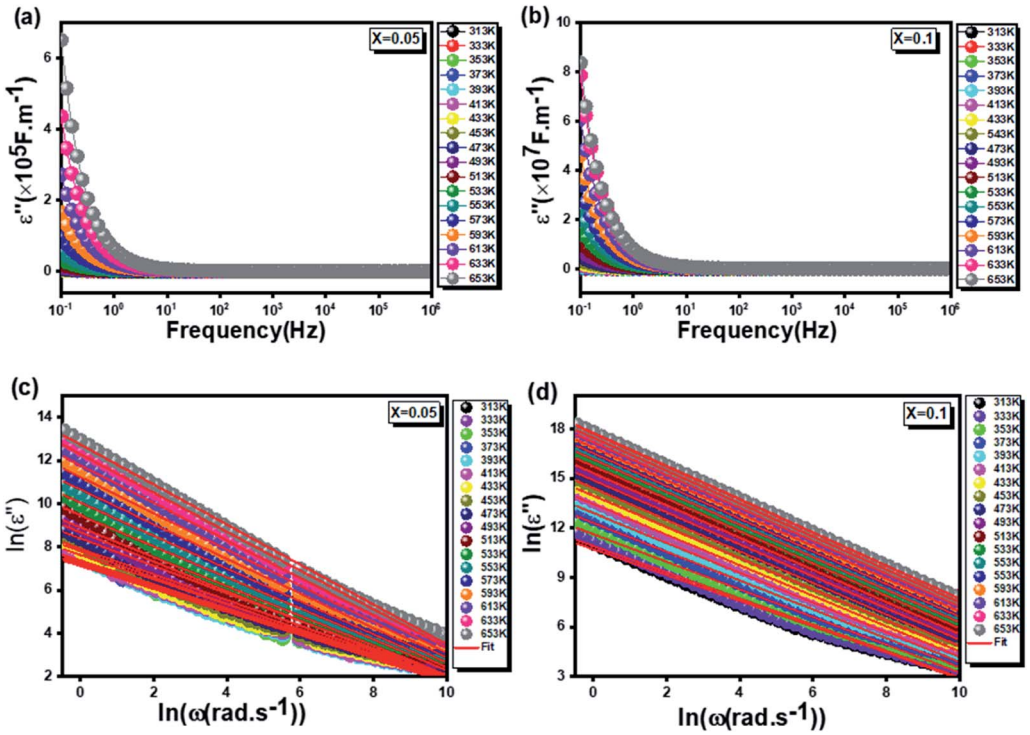

Fig. 6 The variation of the imaginary part of the permittivity as a function of frequency at different temperatures for the $Ag_xZn_{1-x}Al_2O_{4-\frac{x}{2}}$ (x = 0.05 (a) and x = 0.1 (b)) samples, Fig. 6 c and d ln (ε'') as a function of ln(ω) at different temperatures for (x = 0.05 (c) and x = 0.1 (d)).

lattice of grain boundaries, and impurities.[57] The density of material also influences the variation in dielectric losses; for example, high porosity (low density) results in low dielectric constant and higher dielectric losses.[58] The frequency dependence at different temperatures of the loss factor for the two samples is plotted in Fig. 10. Similar to ε', tanδ values are important at low frequencies and gradually reduce at high frequencies until reaching a lower saturated value. The losses are minimized at high frequencies and the dipoles contribute to the polarization because their polarization can orient with the electric field due to their high conductivity.[19,58] Thus, we notice that the value of the dielectric loss increases with an increase in temperature due to the electrical conductivity.[59]

In this context, these results suggest that the two samples can be used in various technological applications, including fuel cells, ceramic technology, and microwave technology.[60]

3.4.4 Modulus analysis. The complex electrical modulus (M*) allows the study of the relaxation process and the dynamics of ions as a function of frequency and temperature.M* can be determined from the dielectric permittivity using the following formula:[61]

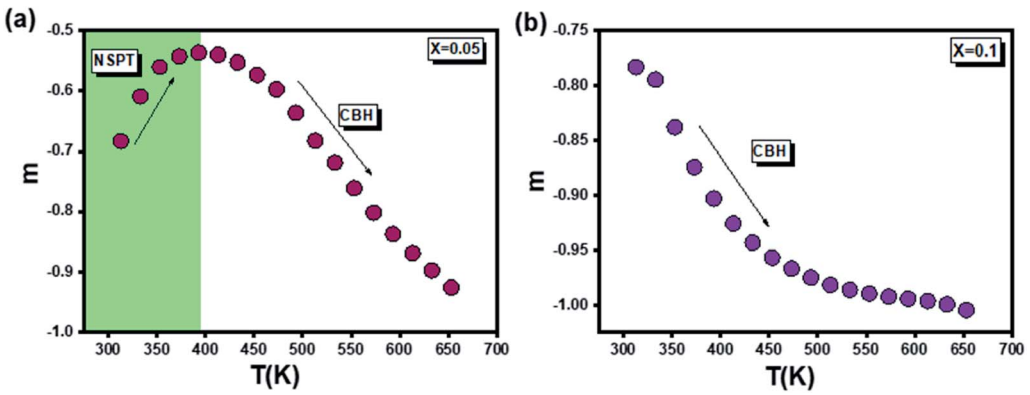

Fig. 7 The exponent (m) calculated as a function of temperature for the $Ag_xZn_{1-x}Al_2O_{4-\frac{x}{2}}$ samples.

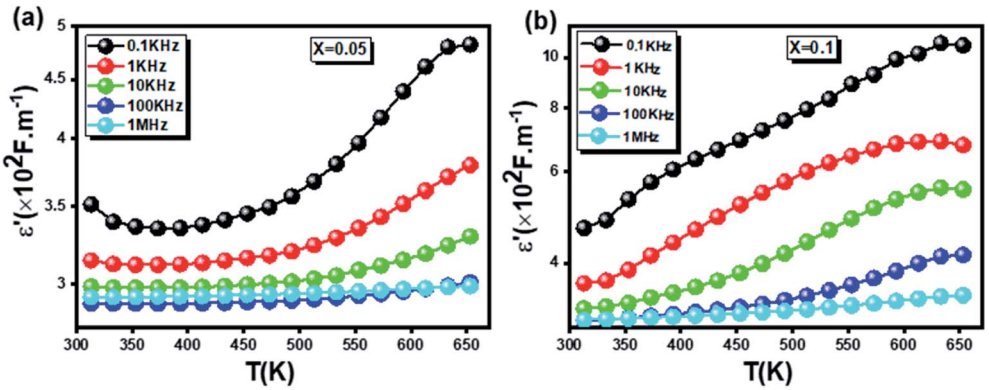

Fig. 8 The real permittivity as a function of temperature at different frequencies (0.1 KHz, 1 KHz, 10 KHz and 1 MHz) for the $Ag_xZn_{1-x}Al_2O_{4-\frac{x}{2}}$ (x = 0.05 (a) and x = 0.1 (b)) samples.

$$M^* = \frac{1}{\varepsilon^*} = M' - iM'' \tag{11}$$

Therefore, the real electric modulus (M′) and the imaginary electric modulus (M″) can be expressed as follow:

$$M' = 2\pi f C_0 Z'' \tag{12}$$

$$M'' = 2\pi f C_0 Z' \tag{13}$$

where: $C_0 = \varepsilon_0.(S/e)$ denotes the cell's vacuum capacitance, ε_0 = 8.854 10^{-12} F m^{-1} is the free space permittivity.

3.4.4.1 Real part of modulus. Fig. 11a and b shows the frequency dependence of the real part (M′) of the complex modulus as a function of frequency at different temperatures of the two prepared compounds.

It is worth noting that the values of M′ curves increase gradually until merging at the high-frequency range for the two compound. This confirms that the electrodes polarization phenomena does not contribute to the relaxation process and can be ignored when the electric field, is evaluated in this form.[62]

3.4.4.2 Imaginary part of modulus. The imaginary part of the electric modulus (M'') as a function of frequency at different temperatures for the two materials is presented in Fig. 12a and b, to better understand dielectric relaxations. All the M'' plots prove a maximum at a specific frequency called the relaxation frequency (f_r). With increasing temperature, this maximum shifted to higher frequencies, implying that the relaxation is as temperature-dependent process.[63] Several research articles[64,65] have also reported similar results. Indeed, at low frequencies, we can see the presence of a pure conduction process[66] in which ions can move freely over long distances. As the M'' peaks move to higher frequencies, the ions are confined to only localized motion, which corresponds to carrier hopping over short distances.[67] The experimental data of the M'' for different temperatures were fitted with an approximate frequency representation of the Kohlrausch–Williams–Watts (KWW) function, proposed by Bergman:[68]

$$M'' = \frac{M''_{\max}}{1-\beta+\left(\frac{\beta}{1+\beta}\right)\left(\beta\left(\frac{f_{\max}}{f}\right)+\left(\frac{f}{f_{\max}}\right)^{\beta}\right)} \tag{14}$$

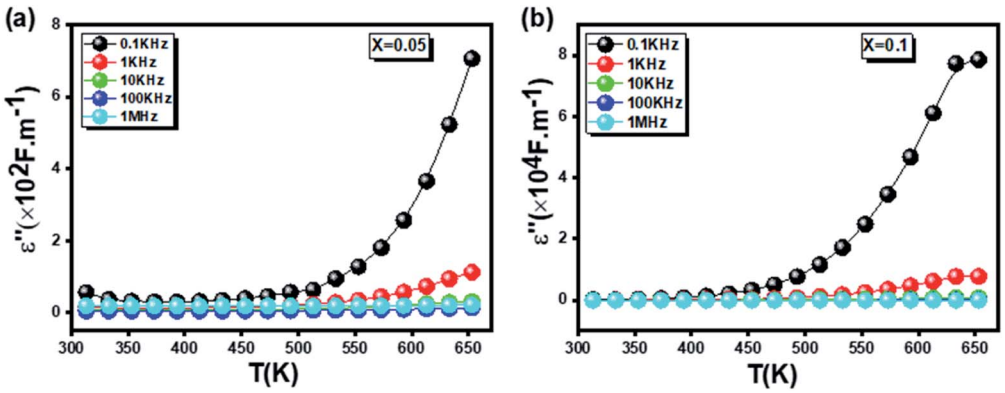

Fig. 9 The temperature dependence of the imaginary permittivity as a function of temperature for the $Ag_xZn_{1-x}Al_2O_{4-\frac{x}{2}}$ (x = 0.05 (a) and x = 0.1 (b)) compounds.

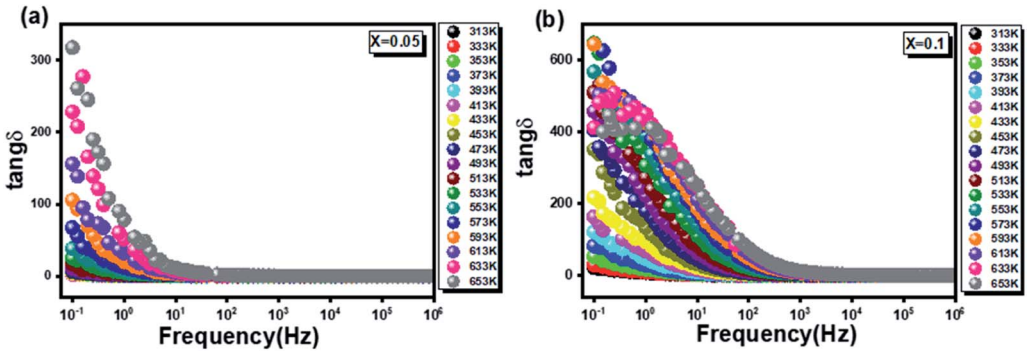

Fig. 10 The frequency dependence at different temperatures of the loss factor for the two $Ag_xZn_{1-x}Al_2O_{4-\frac{x}{2}}$ ($x = 0.05$ (a) and $x = 0.1$ (b)) samples.

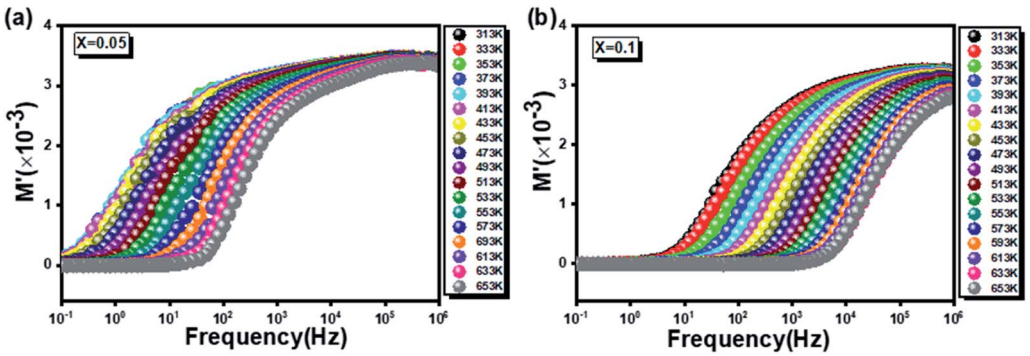

Fig. 11 The frequency dependence of the real part of the complex modulus as a function for the two $Ag_xZn_{1-x}Al_2O_{4-\frac{x}{2}}$ ($x = 0.05$ (a) and $x = 0.1$ (b)) compounds.

where: M_{max}'' is the maximum value of the modulus peak, f_{max} is the M_{max}'' corresponding frequency, and ($0 < \beta < 1$) is the factor that appears in the empirical Kohlrausch function providing information on the type of dielectric relaxation which can be either Debye type or non-Debye type.[69] In another hand, the temperature dependence of β is feature in Fig. 13a and b proving a continuous decrease up to 393 K than an increase for $x = 0.05$ (curve (a)), and for $x = 0.1$ (curve (b)), β behaves and increases with increasing temperature. Furthermore, Fig. 13c and d shows that the theoretical calculation fit agrees well with the experimental data.

When plotting the variation of the relaxation frequency (f_{max}) as a function of the inverse of the absolute temperature (1000/T), as seen in Fig. 14, it should be noted that this variation presents an activated behavior, according to following Arrhenius law:[70]

$$f_{max} = f_0 \exp\left(-\frac{E_a}{K_B T}\right) \quad (15)$$

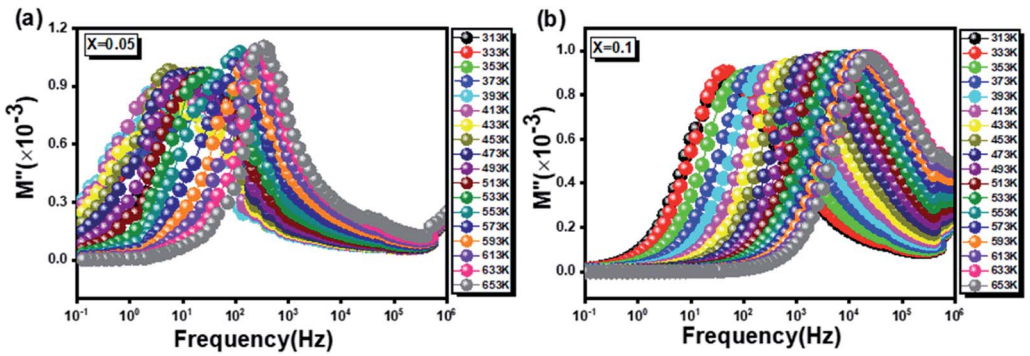

Fig. 12 The imaginary part of the electric modulus as a function of frequency for the $Ag_xZn_{1-x}Al_2O_{4-\frac{x}{2}}$ ($x = 0.05$ (a) and $x = 0.1$ (b)) compounds.

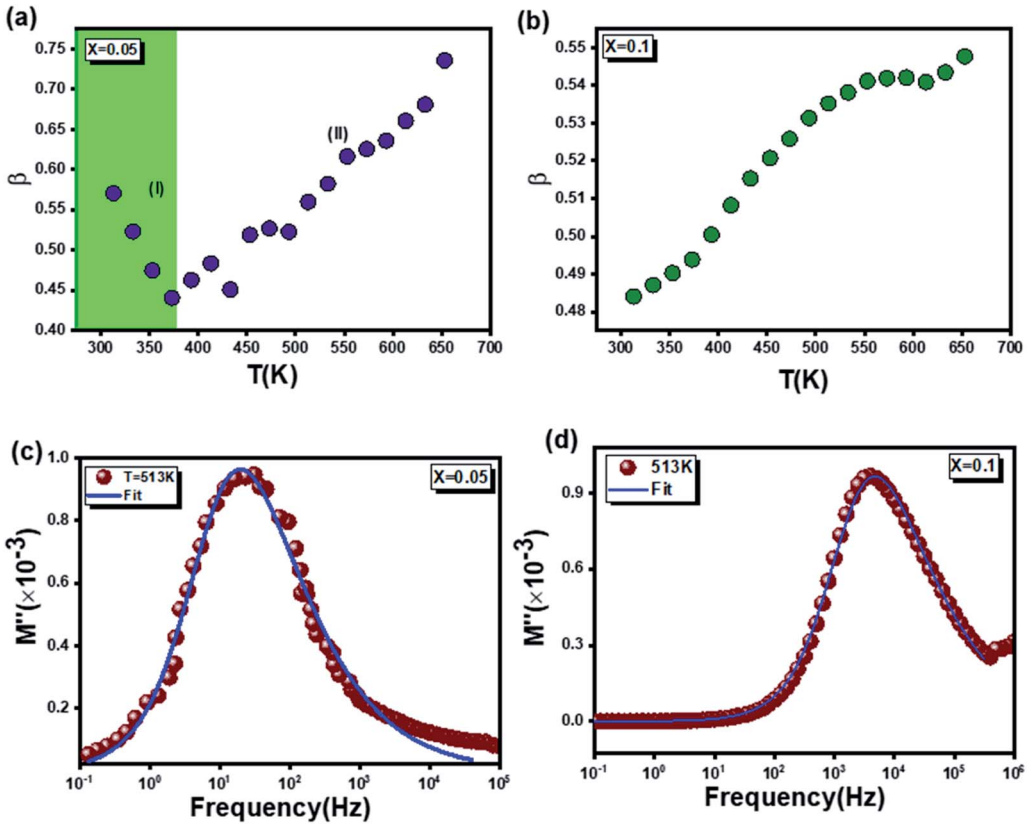

Fig. 13 Temperature dependence of the β value for the two $Ag_xZn_{1-x}Al_2O_{4-\frac{x}{2}}$ ($x = 0.05$ (a) and $x = 0.1$ (b)) compounds. Example adjustment of the (M″) for compounds ($x = 0.05$ (c) and $x = 0.1$ (d)) at $T = 433$ K.

where: K_B is Boltzmann's constant, E_a denotes the activation energy required for the dielectric relaxation, and f_0 is the pre-exponential factor.

The extracted values of the activation energy are: $E_a = 0.610$ eV and $E_a = 0.419$ eV respectively for $x = 0.05$ and $x = 0.1$, proving a decrease with increase in the Ag amount.

3.4.5 Complex polarizability studies. To better understand the phenomena of dielectric relaxation, the complex polarizability (α^*), proposed by Scaife,[71] was then focused, which is defined as follows:

$$\alpha^* = \alpha^* = \alpha' - i\alpha'' = \frac{\varepsilon^* + 1}{\varepsilon^* + 2} \quad (16)$$

Where α' and α'' are the real and imaginary parts of the complex polarizability α^*.

Accordingly, we can easily get the imaginary parts α'' from eqn (16):[50]

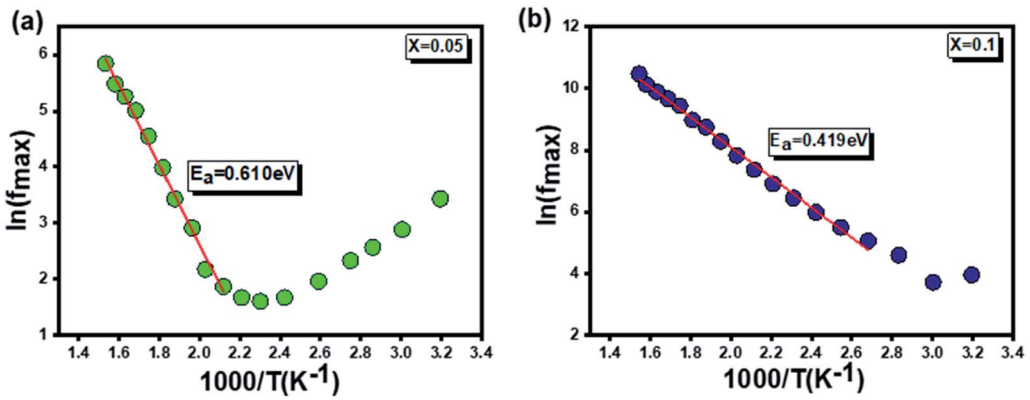

Fig. 14 The variation of the relaxation frequency (f_{max}) as a function of (1000/T) for the two $Ag_xZn_{1-x}Al_2O_{4-\frac{x}{2}}$ ($x = 0.05$ (a) and $x = 0.1$ (b)) compounds.

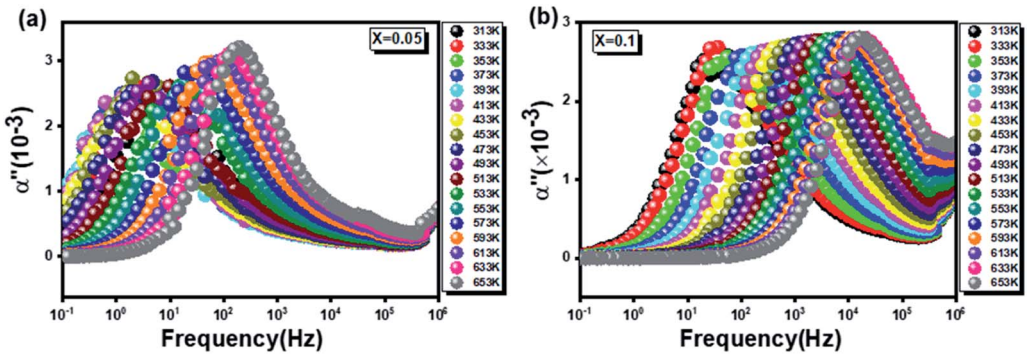

Fig. 15 The imaginary part of complex polarizability as a function of frequency for the $Ag_xZn_{1-x}Al_2O_{4-\frac{x}{2}}$ ($x = 0.05$ (a) and $x = 0.1$ (b)) compounds.

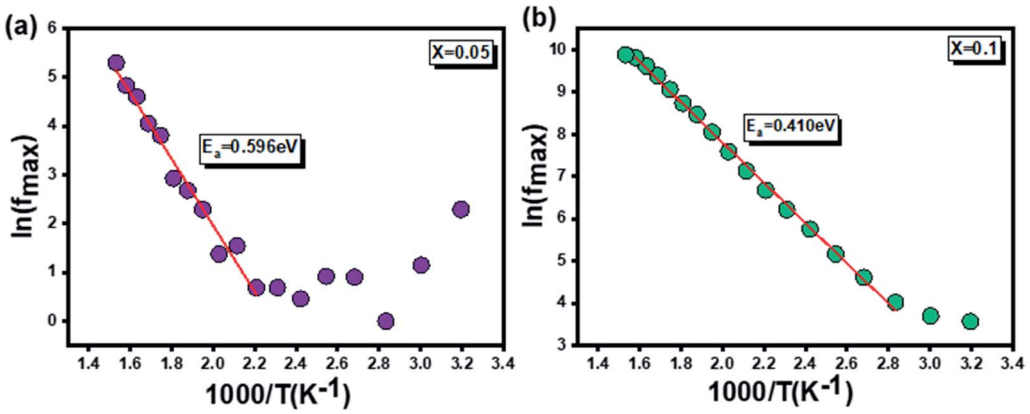

Fig. 16 The variation of (ln (f_{max})) *versus* of (1000/T) for the $Ag_xZn_{1-x}Al_2O_{4-\frac{x}{2}}$ ($x = 0.05$ (a) and $x = 0.1$ (b)) compounds.

$$\alpha'' = \frac{3\varepsilon''}{(\varepsilon' + 2)^2 + \varepsilon''^2} \quad (17)$$

The complex polarizability gives proper weight to all polarization mechanisms and provides an easy way to compare the dielectric behavior of different substances.

On this point, Fig. 15 represents the variation of α'' *versus* frequency at different temperature and highlights that a well separated relaxation peak with a maximum which shifts towards higher frequencies. According to these finding we displayed, in Fig. 16, the plot of (ln (f_{max})) as a function of the inverse temperature of (1000/T).

The extracted activation energies are about is for 0.569 and 0.41 eV respectively for $x = 0.05$ and $x = 0.1$ which are almost the same as those extracted from the module analysis.

4. Conclusion

In summary, we have studied the optical and dielectric properties of $Ag_xZn_{1-x}Al_2O_{4-\frac{x}{2}}$ ($x = 0.05$ and $x = 0.1$) spinels prepared by sol-gel auto-combustion process. Both compounds crystallize in the cubic structure of space group $Fd\bar{3}m$ and exhibit a minority of (Ag) phase, according to the XRD measurements. In addition, FTIR spectroscopy analysis confirmed the formation of spinel structured compounds. The Kubelka–Munk formula is used to calculate the absorption coefficient, where the optical band gap is determined by the Tauc model. The calculated gap energy values are 4.3 eV for $x = 0.05$ and 4 eV for $x = 0.1$, indicating semiconductor behavior for both samples, which are better suited for applications as photodetectors, optoelectronics, and photovoltaics. The activation energies estimated from the modulus were found to be 0.599 eV for $x = 0.05$ and 0.412 eV for $= 0.1$, which is in agreement with the values obtained from the complex polarizability plot, in effect demonstrating that the charge carriers involved in the conduction and relaxation processes are the same.

Conflicts of interest

There are no conflicts to declare.

References

1 E. J. W. Verwey and E. L. Heilmann, *J. Chem. Phys.*, 1947, **15**, 174–180.

2 I. Miron, C. Enache, M. Vasile and I. Grozescu, *Phys. Scr.*, 2012, **2012**, 014064.
3 X. Yong, F. Ping, Z. Baohua, G. Juan, Z. Lin and W. Xuehua, *Mater. Lett.*, 2014, **123**, 142–144.
4 V. Ciupina, I. Carazeanu and G. Prodan, *J. Optoelectron. Adv. Mater.*, 2004, **6**, 1317–1322.
5 M. Kumar, T. K. Seshagiri, M. Mohapatra, V. Natarajan and S. V. Godbole, *J. Lumin.*, 2012, **132**, 2810–2816.
6 F. F. Komahal, H. Nagabhushana, R. B. Basavaraj, G. P. Darshan and B. D. Prasad, *Opt. Mater.*, 2018, **84**, 536–544.
7 M. Kumar, V. Natarajan and S. V. Godbole, *Bull. Mater. Sci.*, 2014, **37**, 1205–1214.
8 P. Fu, Z. Wang, Z. Lin, Y. Liu and V. A. Roy, *J. Mater. Sci.: Mater. Electron.*, 2017, **28**, 9589–9595.
9 S. Siragam, R. S. Dubey and L. Pappula, *Mater. Today: Proc.*, 2021, **45**, 2091–2095.
10 L. Zou, F. Li, X. Xiang, D. G. Evans and X. Duan, *Chem. Mater.*, 2006, **18**, 5852–5859.
11 M.-T. Tsai, Y.-S. Chang, B. Huang and B.-Y. Pan, *Ceram. Int.*, 2013, **39**, 3691–3697.
12 T. K. Parya, R. K. Bhattacharyya, S. Banerjee and U. B. Adhikari, *Ceram. Int.*, 2010, **36**, 1211–1215.
13 M. Zawadzki, *Solid State Sci.*, 2006, **8**, 14–18.
14 H. Agarwal, T. P. Yadav, O. N. Srivastava and M. A. Shaz, *Ceram. Int.*, 2017, **43**, 16986–16992.
15 J. Wrzyszcz, M. Zawadzki, J. Trawczyński, H. Grabowska and W. Miśta, *Appl. Catal., A*, 2001, **210**, 263–269.
16 J. J. Kingsley, K. Suresh and K. C. Patil, *J. Mater. Sci.*, 1990, **25**, 1305–1312.
17 N. Pathak, S. K. Gupta, K. Sanyal, M. Kumar, R. M. Kadam and V. Natarajan, *Dalton Trans.*, 2014, **43**, 9313–9323.
18 Q. Pan, S. Ye, D. Yang, J. Qiu and G. Dong, *Mater. Res. Bull.*, 2017, **93**, 310–317.
19 M. Amghar, A. Bougoffa, A. Trabelsi, A. Oueslati and E. Dhahri, *RSC Adv.*, 2022, **12**, 15848–15860.
20 P. Kumari, Y. Dwivedi and A. Bahadur, *Optik*, 2018, **154**, 126–132.
21 G. T. Anand, L. J. Kennedy, J. J. Vijaya, K. Kaviyarasan and M. Sukumar, *Ceram. Int.*, 2015, **41**, 603–615.
22 W. Staszak, M. Zawadzki and J. Okal, *J. Alloys Compd.*, 2010, **492**, 500–507.
23 R. Ianoş, R. Lazău, I. Lazău and C. Păcurariu, *J. Eur. Ceram. Soc.*, 2012, **32**, 1605–1611.
24 X. Duan, D. Yuan, Z. Sun, H. Sun, D. Xu and M. Lv, *J. Cryst. Growth*, 2003, **252**, 4–8.
25 E. M. A. Jamal, D. S. Kumar and M. R. Anantharaman, *Bull. Mater. Sci.*, 2011, **34**, 251–259.
26 S. V. Motloung, F. B. Dejene, H. C. Swart and O. M. Ntwaeaborwa, *J. Sol-Gel Sci. Technol.*, 2014, **70**, 422–427.
27 S. V. Motloung, M. Tsega, F. B. Dejene, H. C. Swart, O. M. Ntwaeaborwa, L. F. Koao, T. E. Motaung and M. J. Hato, *J. Alloys Compd.*, 2016, **677**, 72–79.
28 A. S. Abu-Khadra, A. M. Taha, A. M. Abdel-Ghany and A. A. Abul-Magd, *Ceram. Int.*, 2021, **47**, 26271–26279.
29 P. Parhi and V. Manivannan, *J. Eur. Ceram. Soc.*, 2008, **28**, 1665–1670.
30 S. Huang, Z. Wei, X. Wu and J. Shi, *J. Alloys Compd.*, 2020, **825**, 154004.
31 T. Sofia Nirmala, N. Iyandurai, S. Yuvaraj and M. Sundararajan, *Mater. Res. Express*, 2020, **7**, 046104.
32 R. Peymanfar and F. Fazlalizadeh, *Chem. Eng. J.*, 2020, **402**, 126089.
33 T. Tangcharoen, J. T-Thienprasert and C. Kongmark, *Int. J. Appl. Ceram. Technol.*, 2021, **18**, 1125–1143.
34 K. Kumar, K. Ramamoorthy, P. M. Koinkar, R. Chandramohan and K. Sankaranarayanan, *J. Nanopart. Res.*, 2007, **9**, 331–335.
35 K. Kumar, K. Ramamoorthy, P. M. Koinkar, R. Chandramohan and K. Sankaranarayanan, *J. Cryst. Growth*, 2006, **289**, 405–407.
36 H. Noor, S. Riaz, M. M. Iram, A. Siddiqi and S. Naseem, Key Engineering Materials, *Trans Tech Publ*, 2018, **778**, 217–224.
37 F. Z. Akika, M. Benamira, H. Lahmar, A. Tibera, R. Chabi, I. Avramova, Ş. Suzer and M. Trari, *J. Photochem. Photobiol., A*, 2018, **364**, 542–550.
38 M. G. Moustafa, H. Morshidy, A. R. Mohamed and M. M. El-Okr, *J. Non-Cryst. Solids*, 2019, **517**, 9–16.
39 H. Y. Morshidy, Z. M. Abd El-Fattah, A. A. Abul-Magd, M. A. Hassan and A. R. Mohamed, *Opt. Mater.*, 2021, **113**, 110881.
40 J. Massoudi, M. Smari, K. Nouri, E. Dhahri, K. Khirouni, S. Bertaina and L. Bessais, *RSC Adv.*, 2020, **10**, 34556–34580.
41 P. Chand, S. Vaish and P. Kumar, *Phys. B*, 2017, **524**, 53–63.
42 P. Herve and L. K. J. Vandamme, *Infrared Phys. Technol.*, 1994, **35**, 609–615.
43 M. A. Ahmed, N. Okasha and R. M. Kershi, *Mater. Chem. Phys.*, 2009, **113**, 196–201.
44 A. Zaouali, A. Dhahri, A. Boughariou, E. Dhahri, R. Barillé, B. F. O. Costa and K. Khirouni, *J. Mater. Sci.: Mater. Electron.*, 2021, **32**, 1221–1232.
45 I. S. Yahia, N. A. Hegab, A. M. Shakra and A. M. Al-Ribaty, *Phys. B*, 2012, **407**, 2476–2485.
46 S. G. Kakade, Y.-R. Ma, R. S. Devan, Y. D. Kolekar and C. V. Ramana, *J. Phys. Chem. C*, 2016, **120**, 5682–5693.
47 N. Assoudi, W. Hzez, R. Dhahri, I. Walha, H. Rahmouni, K. Khirouni and E. Dhahri, *J. Mater. Sci.: Mater. Electron.*, 2018, **29**, 20113–20121.
48 J. C. Giuntini, J. V. Zanchetta, D. Jullien, R. Eholie and P. Houenou, *J. Non-Cryst. Solids*, 1981, **45**, 57–62.
49 M. A. M. Seyam, *Appl. Surf. Sci.*, 2001, **181**, 128–138.
50 Y. B. Taher, A. Oueslati, K. Khirouni and M. Gargouri, *J. Cluster Sci.*, 2015, **26**, 1655–1669.
51 F. B. Abdallah, A. Benali, S. Azizi, M. Triki, E. Dhahri, M. P. F. Graça and M. A. Valente, *J. Mater. Sci.: Mater. Electron.*, 2019, **30**, 8457–8470.
52 R. Hamdi, J. Khelifi, I. Walha, W. Hzez and E. Dhahri, *J. Low Temp. Phys.*, 2021, **203**, 158–179.
53 F. B. Abdallah, A. Benali, S. Azizi, M. Triki, E. Dhahri, M. P. F. Graça and M. A. Valente, *J. Mater. Sci.: Mater. Electron.*, 2019, **30**, 8457–8470.

54 I. Soibam, S. Phanjoubam, H. B. Sharma, H. N. K. Sarma, R. Laishram and C. Prakash, *Solid State Commun.*, 2008, **148**, 399–402.
55 S. A. Saafan and S. T. Assar, *J. Magn. Magn. Mater.*, 2012, **324**, 2989–3001.
56 S. Saha and T. P. Sinha, *J. Appl. Phys.*, 2006, **99**, 014109.
57 M. Z. Ahsan and F. A. Khan, *J. Phys. Sci.*, 2017, **7**, 30–37.
58 R. V. Mangalaraja, P. Manohar, F. D. Gnanam and M. Awano, *J. Mater. Sci.*, 2004, **39**, 2037–2042.
59 S. Gowreesan and A. Ruban Kumar, *Appl. Phys. A:*, 2017, **123**, 1–8.
60 A. Hadded, J. Massoudi, E. Dhahri, K. Khirouni and B. F. O. Costa, *RSC Adv.*, 2020, **10**, 42542–42556.
61 A. E. Stearn and H. Eyring, *J. Chem. Phys.*, 1937, **5**, 113–124.
62 H. Lin, R. P. Hania, R. Bloem, O. Mirzov, D. Thomsson and I. G. Scheblykin, *Phys. Chem. Chem. Phys.*, 2010, **12**, 11770–11777.
63 J. S. Kim, *J. Phys. Soc. Jpn.*, 2001, **70**, 3129–3133.
64 A. Dutta, T. P. Sinha and S. Shannigrahi, *Phys. Rev. B*, 2007, **76**, 155113.
65 P. Victor, S. Bhattacharyya and S. B. Krupanidhi, *J. Appl. Phys.*, 2003, **94**, 5135–5142.
66 K. Holderna-Natkaniec, M. O. M. Sghaier, P. Lawniczak, M. Zdanowska-Frączek, A. Wozniak-Braszak and S. Chaabouni, *Polyhedron*, 2015, **85**, 131–136.
67 A. Bougoffa, A. Benali, M. Bejar, E. Dhahri, M. P. F. Graça, M. A. Valente, L. Bessais and B. O. F. Costa, *J. Alloys Compd.*, 2021, **856**, 157425.
68 A. Bougoffa, J. Massoudi, M. Smari, E. Dhahri, K. Khirouni and L. Bessais, *J. Mater. Sci.: Mater. Electron.*, 2019, **30**, 21018–21031.
69 K. S. Rao, P. M. Krishna, D. M. Prasad and D. Gangadharudu, *J. Mater. Sci.*, 2007, **42**, 4801–4809.
70 E. M. Benali, A. Benali, M. Bejar, E. Dhahri, M. P. F. Graca, M. A. Valente and B. F. O. Costa, *J. Mater. Sci.: Mater. Electron.*, 2020, **31**, 3197–3214.
71 B. K. P. Scaife, *Proc. Phys. Soc.*, 1963, **81**, 124.